American Journal of Computational Mathematics, 2025, 15(4), 506-532
https://www.scirp.org/journal/ajcm
ISSN Online: 2161-1211
ISSN Print: 2161-1203

Optimization of MHD Natural Convection in a Wavy Square Enclosure with Semicircular Heater Using RSM and Al-Water Nanofluid

Mohammad Mahfuzul Islam[1], Md. Yousuf Ali[2], Md. Abdul Alim[2*], Md. Mahmud Alam[1]

[1]Department of Mathematics, Dhaka University of Engineering and Technology, Gazipur, Bangladesh
[2]Department of Mathematics, Bangladesh University of Engineering and Technology, Dhaka, Bangladesh
Email: mahfuzabir@gmail.com, yousufmath33@gmail.com, *maalim@math.buet.ac.bd, alamdr.mahmud@duet.ac.bd

How to cite this paper: Islam, Md.M., Ali, Md.Y., Alim, Md.A. and Alam, Md.M (2025) Optimization of MHD Natural Convection in a Wavy Square Enclosure with Semicircular Heater Using RSM and Al-Water Nanofluid. *American Journal of Computational Mathematics*, **15**, 506-532.
https://doi.org/10.4236/ajcm.2025.154023

Received: October 13, 2025
Accepted: December 19, 2025
Published: December 22, 2025

Abstract

The present study investigates magnetohydrodynamic (MHD) natural convection of Al_2O_3-water nanofluid in a wavy square cavity containing a heated semicircular obstacle using the Finite Element Method (FEM). The top wavy wall of the cavity is maintained at a cold temperature (T_c), while the bottom wall and semicircular obstacle are heated to a higher temperature (T_h), with the vertical walls kept thermally insulated. Parametric analysis is carried out for Rayleigh numbers in the range of $10^3 \le Ra \le 10^5$, nanoparticle volume fractions $0 \le \varphi \le 0.05$, and Hartmann numbers $0 \le Ha \le 100$. Flow structures and heat transport are illustrated through streamlines, isotherms, velocity, and temperature profiles, along with the average Nusselt number. Results show that increasing Ra enhances buoyancy-driven convection and improves heat transfer, while higher nanoparticle volume fractions (φ) further augment the thermal performance due to enhanced conductivity of the nanofluid. In contrast, stronger magnetic fields (higher Ha) suppress convective circulation and reduce heat transfer rates. A maximum enhancement of approximately 19.8% in Nu_{av} is observed at $\varphi = 0.05$ compared with the base fluid, whereas heat transfer decreases noticeably with increasing Ha. The combined effects of cavity geometry, nanoparticle loading, and magnetic field highlight the complex interplay between buoyancy and Lorentz forces, offering valuable insights for the design of thermally efficient nanofluid-based systems.

Keywords

Free Convection, Nanofluid, Magnetic Field, Wavy Cavity, Finite Element Method

1. Introduction

Natural convective heat transfer has attracted significant attention from researchers due to its wide range of practical applications, including heat exchangers, building heating and cooling systems, nuclear reactors, solar collectors, electrical equipment, fire safety, and petrochemical processes. Its popularity stems from the simplicity and low cost of constructing geometrical domains, despite convection occurring through both natural and forced mechanisms. Natural convection arises primarily from temperature differences and buoyancy forces, and its simplicity and broad applicability have made it the subject of numerous studies [1]-[4]. Nanofluids, engineered suspensions of nanoparticles such as Al_2O_3, CuO, TiO_2, or Ag in base fluids like water, ethylene glycol, or oils, have emerged as a powerful approach for enhancing heat transfer in thermal systems. Their introduction was motivated by the need to improve thermal conductivity and heat transfer coefficients beyond those achievable with conventional fluids. Putra *et al.* [5] carried out one of the early investigations on natural convection in nanofluids, showing that particle addition altered flow structures and improved thermal transport. An expression for the viscosity of solutions and suspensions at finite concentrations is derived by analyzing the incremental effect of adding a solute molecule to a continuous medium representing the existing solution by Brinkman [6]. Later numerical and experimental works further confirmed the potential of nanofluids. Nada *et al.* [7] investigated heat transfer enhancement in a differentially heated enclosure using variable thermal conductivity and viscosity models for Al_2O_3-water and CuO-water nanofluids across a wide range of Rayleigh numbers, nanoparticle volume fractions, and aspect ratios, revealing the sensitivity of the Nusselt number to nanoparticle concentration, aspect ratio, and viscosity model selection. Nasrin *et al.* [8] explored numerical investigation of steady laminar combined convection in a vertical triangular wavy enclosure filled with water-CuO nanofluid using the Brinkman and Pak-Cho models, highlighting the influence of Reynolds number, Richardson number, and nanoparticle volume fraction on flow and heat transfer characteristics, with significant enhancement observed due to nanoparticle inclusion. Parvin *et al.* [9] studied natural convection in a complex enclosure with a heated diamond-shaped obstacle filled with Cu-water nanofluid, revealing that increasing the Prandtl number enhances the heat transfer rate.

Zahan *et al.* [10] demonstrated the numerical investigation of MHD conjugate natural convection in a rectangular enclosure filled with Cu-water nanofluid reveals that heat transfer improves with increasing Rayleigh number and nanoparticle volume fraction, but decreases with higher Hartmann numbers. Similarly, Alsabery *et al.* [11] analyzed natural convection in a square cavity containing a corner heater and a conducting solid block, using a two-phase Al_2O_3-water nanofluid model, and reveals that higher solid block thermal conductivity enhances conduction-dominated heat transfer. Saha *et al.* [12] investigated the MHD free convection in a square cavity with a wavy top wall and a centrally located heated vertical fin filled with Al_2O_3-H_2O nanofluid revealing that heat trans-

fer increases with higher Rayleigh number, Hartmann number, and nanoparticle volume fraction, and is significantly affected by the nanoparticle shape. Rashid *et al.* [13] examined lid-driven cavity flow with a central heated circular obstacle using diamond water nanofluid, demonstrating that nanoparticle shape significantly influences heat transfer, with lamina-shaped particles outperforming spherical and columnar shapes in enhancing temperature distribution and Nusselt number.

The entropy generation minimization method is applied to MHD flow between two finite-conductivity parallel walls, showing that asymmetric convective cooling of the walls minimizes total irreversibility from heat conduction, viscosity, and Joule dissipation discussed by Ibanz G. *et al.* [14]. Geometric design is central in cavity convection problems. Wavy or corrugated cavity walls increase the effective heat transfer surface and disturb boundary layer development, typically enhancing convective heat transport compared to flat cavities. Islam *et al.* [15] visualized heatline distributions in prismatic enclosures with MHD effects, highlighting the strong role of geometry and boundary conditions in shaping flow patterns. MHD free convection in a square cavity with a heated bottom wall and cooled side and top walls shows that temperature distribution, flow patterns, and heat transfer are influenced by Rayleigh and Hartmann numbers, with magnetic fields reducing convection intensity and flow velocity conducted numerically by Jani *et al.* [16].

Due to their significantly enhanced thermal properties, nanofluids have received extensive attention in recent decades. Their superior thermal conductivity and altered viscosity have expanded their potential for improved heat transfer performance. Numerous researchers have developed empirical correlations for these properties based on experimental data to better predict heat transfer behavior. Einstein [17] and Batchelor [18] have proposed various correlations to estimate the absolute viscosity of nanofluids, accounting for the nanoparticle volume fraction as a key variable. Additionally, several studies have introduced empirical models to predict the thermal conductivity of nanofluids. Xu *et al.* [19] introduced an improved steady-flow technique to measure the thermal conductivity of nanofluids and found that Al_2O_3-water nanofluids offer significant thermal performance enhancement even at low nanoparticle volume fractions. Raja and Sunil [20] evaluated the thermal conductivity of nanofluids using various existing models and emphasized the need for further research to identify the most suitable model for specific applications. The single-phase nanofluid model neglects slip mechanisms such as Brownian motion and thermophoresis between the nanoparticles and the base fluid, which may reduce accuracy at higher particle loadings. However, for dilute concentrations ($\varphi \leq 0.05$), these slip effects are minimal, and the single-phase approach provides reliable predictions while maintaining lower computational complexity compared to two-phase or slip models.

Recently, the use of the Response Surface Methodology (RSM) has gained momentum for analyzing the sensitivity of thermal transport phenomena. Response Surface Methodology (RSM) is a statistical modeling technique that employs

mathematical relationships to describe the interactions between system inputs and outputs by Jahan *et al.* [21]. Its capability to capture nonlinear dependencies makes it effective for modeling the thermophysical properties of nanofluids Zheng *et al.* [22]. Although numerous studies have examined MHD natural convection in closed cavities, only a limited number have recently focused on wavy enclosures incorporating different types of nanoparticles [23] [24]. Vahedi *et al.* [25] developed Response Surface Methodology (RSM) to optimize MHD flow around and through a porous cylinder, identifying that Reynolds and Stuart numbers significantly influence heat transfer and drag.

Although considerable progress has been achieved in understanding nanofluid natural convection, magnetohydrodynamic (MHD) effects, and cavity geometries individually, relatively few studies have simultaneously integrated all these aspects. In particular, the combined influence of Al_2O_3-water nanofluid within a wavy cavity geometry featuring an embedded semicircular heater under MHD effects has received limited attention. Moreover, the application of response surface methodology (RSM)-based optimization in such configurations remains largely unexplored. To address this gap, the present study employs finite element method (FEM) simulations coupled with a central composite design (CCD)-based RSM to evaluate the individual and interactive effects of the Rayleigh number (*Ra*), Hartmann number (*Ha*), and nanoparticle volume fraction (ϕ) on the average Nusselt number, thereby offering both numerical insights and optimization guidelines.

2. Mathematical Framework

2.1. Physical Description

In this study, a wavy square enclosure inside a triangular heater is occupied as a domain full of Aluminum Oxide (Al_2O_3) nanoparticles with water (H_2O), which is taken incompressible laminar fluid, time-independent, Newtonian, and steady 2D mixed convective flow with a magnetic field. A wavy enclosure insulated hollow measuring L in length and H in height, with a semicircular heater. The physical shape of this shape using a nanofluid model is shown in **Figure 1**. Engaged to be a cooled surface, T_c is the two sides wall and top wavy wall, while a heated surface T_h, is thought to be the bottom wall and semicircular heater. The fluid domain's exterior, protected boundaries remain intact. Furthermore, the acceleration owing to gravity, g, operates in the opposite direction of the Y axis. A constant magnetic field B_0 also exists surrounding the container, running from right to left. Furthermore, the neighboring media being considered no slip, the size and shape of the Al_2O_3 nanoparticles are assumed to be the same. The thermophysical characteristics of the considered nanofluid in this case are shown in **Table 1**. The fluid flow segment appears and is completed using a two-dimensional Cartesian arrangement, with the left wall marked by the Y-direction and the bottom wall denoted by the X-direction.

2.2. Governing Equations

The connected governing equations for this two-dimensional steady natural con-

vection wavy enclosure with MHD interference are as follows [27].

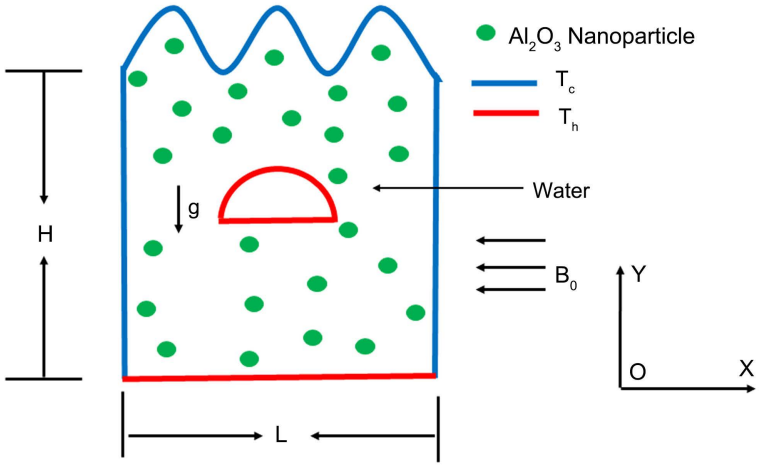

Figure 1. The physical representation of the proposed investigation.

Table 1. Relevant thermophysical data for the base fluid and solid particles [26].

Base fluid & Nanoparticle	ρ (Kg·m^{-3})	c_p (J·Kg^{-1}·K^{-1})	κ (W·m^{-1}·K^{-1})	σ (S·m^{-1})	β (K^{-1})	μ (Kg·m^{-1}·s^{-1})	Pr
H_2O	997.1	4179	0.613	5.5×10^{-6}	2.1×10^{-4}	8.91×10^{-4}	6.9
Al_2O_3	3970	765	40	3.69×10^{7}	0.85×10^{-5}	-	-

Continuity Equation:

$$\frac{\partial u}{\partial x}+\frac{\partial v}{\partial y}=0 \tag{1}$$

Momentum Equation:

$$\rho_{nf}\left(u\frac{\partial u}{\partial x}+v\frac{\partial u}{\partial y}\right)=-\frac{\partial p}{\partial x}+\mu_{nf}\left(\frac{\partial^2 u}{\partial x^2}+\frac{\partial^2 u}{\partial y^2}\right) \tag{2}$$

$$\rho_{nf}\left(u\frac{\partial v}{\partial x}+v\frac{\partial v}{\partial y}\right)=-\frac{\partial p}{\partial y}+\mu_{nf}\left(\frac{\partial^2 v}{\partial x^2}+\frac{\partial^2 v}{\partial y^2}\right)+\left(\rho\beta\right)_{nf} g\left(T-T_c\right)-\sigma_{nf}B_0^2 v \tag{3}$$

Energy Equation:

$$u\frac{\partial T}{\partial x}+v\frac{\partial T}{\partial y}=\alpha_{nf}\left(\frac{\partial^2 T}{\partial x^2}+\frac{\partial^2 T}{\partial y^2}\right) \tag{4}$$

Where the velocity component (u,v) is performed through the X and Y axes in this instance, correspondingly. In the momentum equation, the buoyancy forces and magnetic field are regarded as body forces (F) acting across the Y-axis. Therefore, in the Y-momentum equation, $F=g\left(\rho\beta\right)_{nf}\left(T-T_c\right)-\sigma_{nf}B_0^2 v$ is replaced.

2.3. Boundary Conditions

The conditions for the boundaries of this fluid domain are defined as follows:

$$\left.\begin{array}{l} u=0, v=0, T=T_h \text{ on botom wall and semicircular obstacle} \\ u=0, v=0, T=T_c \text{ on two sides wall} \\ u=0, v=0, T=T_c \text{ on top wavy wall} \end{array}\right\} \quad (5)$$

2.4. Features of Nanofluids

The present subsection outlines the thermo-physical properties of the base fluid (H_2O) and the nanoparticles (Al_2O_3). The characteristics of the nanofluid are primarily influenced by those of its base fluid and nanoparticles. Accordingly, the regression coefficients provided in Table 2 are applied to estimate the nanofluid's properties. The viscosity of the Al_2O_3-H_2O nanofluid is determined using the empirical correlation proposed by Islam [27]. The Brinkman and Maxwell correlations are used for effective viscosity and thermal conductivity, respectively, as they are well-established for dilute, spherical, and uniformly dispersed nanoparticle suspensions ($\varphi \le 0.05$). These models assume negligible particle interactions and no slip; deviations such as higher φ or agglomeration may introduce uncertainties, but their influence is minimal at the present low concentration.

Table 2. The interaction model relating the nanoparticles and the base fluid in the nanofluid formulation is employed as proposed in [27] [28].

Nanofluid Properties	Applied Models
Density	$\rho_{nf} = (1-\phi)\rho_f + \phi\rho_s$
Viscosity	$\mu_{nf} = \dfrac{\mu_f}{(1-\phi)^{2.5}}$, (Brinkman model. [6])
Heat Capacitance coefficient	$(\rho C_p)_{nf} = (1-\phi)(\rho C_p)_f + \phi(\rho C_p)_s$
Thermal Expansion	$(\rho\beta)_{nf} = (1-\phi)(\rho\beta)_f + \phi(\rho\beta)_s$
Thermal Conductivity:	$\dfrac{k_{nf}}{k_f} = \dfrac{k_s + 2k_f - 2(k_f - k_s)\phi}{k_s + 2k_f + (k_f - k_s)\phi}$, (Maxwell Model. [29])
Electrical Conductivity	$\dfrac{\sigma_{nf}}{\sigma_f} = \dfrac{\sigma_s + 2\sigma_f - 2(\sigma_f - \sigma_s)\phi}{\sigma_s + 2\sigma_f + (\sigma_f - \sigma_s)\phi}$, (Maxwell Model. [29])

2.5. Non-Dimensional Analysis

For dimensionless the above equations now using the following variables:

$$\left.\begin{array}{l} X = \dfrac{x}{L}, Y = \dfrac{y}{L}, U = \dfrac{uL}{\alpha_f}, V = \dfrac{vL}{\alpha_f}, P = \dfrac{pL^2}{\rho_f \alpha_f^2}, \theta = \dfrac{T - T_c}{T_h - T_c}, \\ Ha = B_0 L\sqrt{\dfrac{\sigma_f}{\mu_f}}, Ra = \dfrac{g\beta_f (T_h - T_c)L^3}{\nu_f \alpha_f} \text{ and } pr = \dfrac{\nu_f}{\alpha_f} \end{array}\right\} \quad (6)$$

Then equations converted into the given below:

$$\frac{\partial U}{\partial X} + \frac{\partial V}{\partial Y} = 0 \quad (7)$$

$$U\frac{\partial U}{\partial X}+V\frac{\partial U}{\partial Y}=-\frac{\rho_f}{\rho_{nf}}\frac{\partial P}{\partial X}+Pr\left(\frac{\mu_{nf}}{\mu_f}\right)\left(\frac{\rho_f}{\rho_{nf}}\right)\nabla^2 U \tag{8}$$

$$\begin{aligned}U\frac{\partial V}{\partial X}+V\frac{\partial V}{\partial Y}=&-\frac{\rho_f}{\rho_{nf}}\frac{\partial P}{\partial Y}+Pr\left(\frac{\mu_{nf}}{\mu_f}\right)\left(\frac{\rho_f}{\rho_{nf}}\right)\nabla^2 V\\&+\frac{(\rho\beta)_{nf}}{\rho_{nf}\beta_f}RaPr\theta-\left(\frac{\rho_f}{\rho_{nf}}\right)\left(\frac{\sigma_{nf}}{\sigma_f}\right)Ha^2 PrV\end{aligned} \tag{9}$$

$$U\frac{\partial \theta}{\partial X}+V\frac{\partial \theta}{\partial Y}=\left(\frac{\alpha_{nf}}{\alpha_f}\right)\nabla^2\theta \tag{10}$$

Then the dimensional boundary conditions are:

On the bottom wall $U=V=0$, $\theta=1$.

On semi-circular obstacle $\theta=1$.

On two sides wall and the wavy top wall $\theta=0$.

2.6. Computation of Physical and Hydrodynamic Parameters

The local Nusselt number (Nu) is used to express the heat transfer coefficient as follows: $Nu=-\frac{k_{nf}}{k_f}\frac{\partial\theta}{\partial\eta}$; where η be the outward drawn normal on the plane and the dimensionless normal temperature gradient is

$$\frac{\partial\theta}{\partial\eta}=\sqrt{\left(\frac{\partial\theta}{\partial X}\right)^2+\left(\frac{\partial\theta}{\partial Y}\right)^2} \tag{11}$$

The average Nusselt number is,

$$\overline{Nu}=-\frac{1}{L}\frac{k_{nf}}{k_f}\int_0^L\frac{\partial\theta}{\partial\eta}\mathrm{ds} \tag{12}$$

Here, S denotes the nondimensional coordinate measured along the circular surface. If $L=1$ for length of the cavity then

$$\overline{Nu}=-\frac{k_{nf}}{k_f}\int_0^1\frac{\partial\theta}{\partial\eta}\mathrm{ds} \tag{13}$$

The effective density, volumetric thermal expansion coefficient, and heat capacitance of the Al_2O_3-water nanofluid are determined using Eqs. (1)-(4), while Eqs. (5)-(13) are employed to evaluate.

3. Numerical Analysis

3.1. Solution Methodology

The system of global nonlinear equations in matrix form was solved using the Newton-Raphson iterative method through a COMSOL Multiphysics solver. Convergence was achieved when the relative error between successive iterations for each variable fell below the specified tolerance ε,

$$\left|\psi^{n+1}-\psi^n\right|<\varepsilon, \tag{14}$$

as defined in Equation (14), where n represents the number of iterations.

The Finite Element Method (FEM) offers significant advantages over other numerical techniques, as it formulates equations element-wise, allowing easy mesh refinement and adaptation. Owing to its capability to handle complex geometries, FEM is widely used for boundary value problems in engineering. The Galerkin Weighted Residual Finite Element Method (GWRFEM) is described in detail in [26], and its computational flow is illustrated in Figure 2.

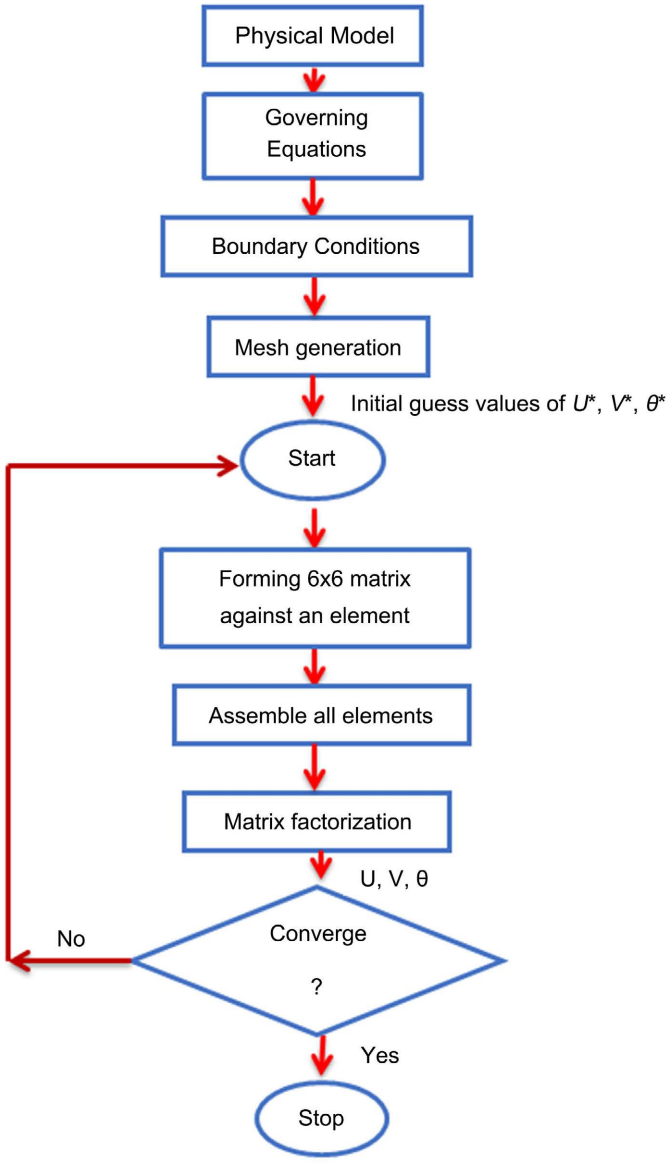

Figure 2. A detailed schematic outlining the steps of the computational approach.

3.2. Grid Sensitivity Analysis

A grid test is described by obtaining the corresponding parameters $Pr = 6.9$, $Ra = 1000$, $Ha = 10$ and $\phi = 0.01$ to acquire the maximum elements feasible using this finite element technique. Additionally, the ideal value of the Nu_{av} is selected to

apply this sensitivity test and create appropriate meshing. This fluid model's entire domain is discretized into six separate numbers (798, 2179, 3402, 8451, 20,963 and 26,310) of triangular elements. An illustration of triangle-style meshing is shown in Figure 3(a). Nu_{av} values for different numbers of triangle members in this fluid domain are also displayed in Table 3. From Figure 3(b) it's clear that the Nu_{av} value for 20,963 elements is practically the same as the value discovered for the following higher number of components. The 20,963 triangular elements are therefore recommended for meshing and finishing this nanofluid model.

Table 3. Numerical values of Nu_{av} for different elements.

Elements	798	2179	3402	8451	20,963	26,310
Nu_{av}	4.1321	4.8132	5.1301	5.8251	6.3543	6.3564
Time (s)	11	24	19	16	22	24

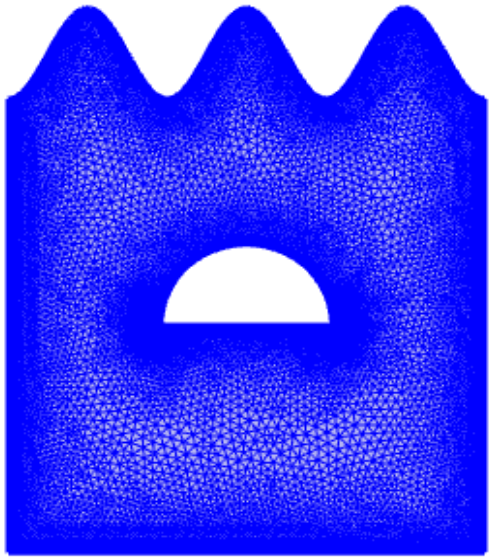

(a)

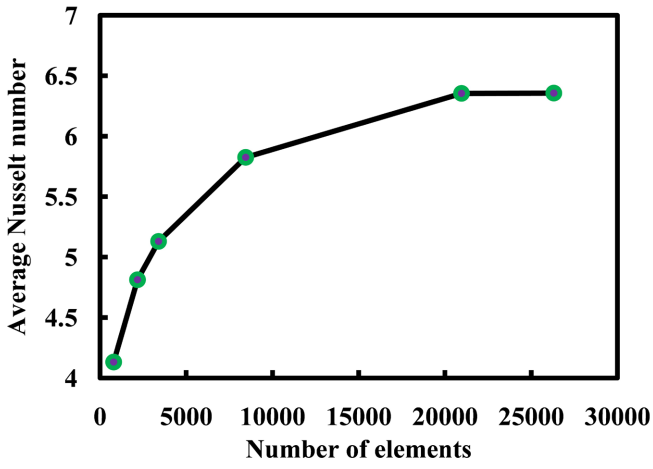

(b)

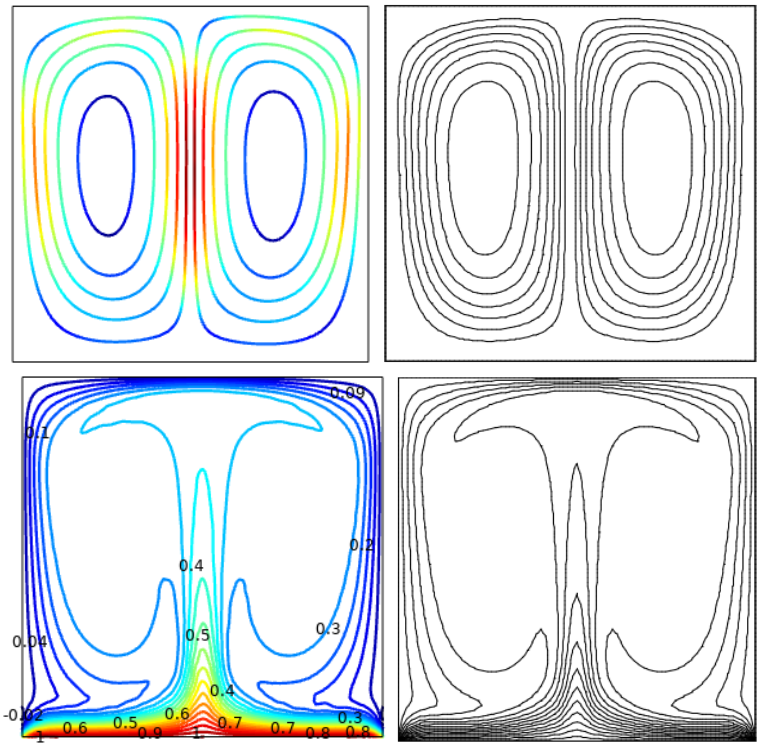

Present work Jani *et al.* [16]

(c)

Figure 3. (a) Meshing type for present simulation, (b) The grid sensitivity test, (c) Comparison results for Streamlines & Isotherms while $Ha = 0$, $Pr = 0.71$ & $Ra = 10^6$.

3.3. Code Validation

The numerical technique was validated through a comparison of streamlines and isotherms with the results displayed in **Figure 3(c)** by Jani *et al.* [16]. They investigate the effect of magnetic field in a square cavity with semi-circular heated block. From these figures as seen the obtained outcomes where $Ha = 0$, $Pr = 0.71$ and $Ra = 10^4$ show excellent agreement. The streamlines and isotherms closely resemble the present outcome.

Table 4. Comparing various Rayleigh numbers utilizing Nu_{av}.

Ra	Φ = 0			Φ = 0.02	
	Ghasemi *et al.* [30]	Islam *et al.* [15]	Present Study	Islam *et al.* [15]	Present Study
10^3	1.002	1.002	1.003	1.060	1.062
10^4	1.183	1.182	1.183	1.208	1.210
10^5	3.150	3.138	3.145	3.097	3.099
10^6	7.907	7.820	7.870	7.796	7.794

In order to validate their code, Ghasemi *et al.* [30] and Islam *et al.* [15] compared the findings with the data that were accessible. As a consequence, the study's numerical methodology is verified by contrasting the current findings with the

results that have been published where Table 4 shows that there is reasonable agreement.

4. Results Discussion

The results of this investigation into MHD natural convection in a wavy square enclosure with a semicircular heater using Aluminum water nanofluid are described using streamlines, isotherms, and Nu_{av}, utilizing $Ra = 1000$, $Pr = 6.9$, $Ha = 10$, and $\phi = 0.01$ as standards. The physical interpretation of the influence of Ra, Ha, and ϕ is demonstrated.

A graphic is used to illustrate the significance of incorporating nanoparticles into a base fluid. Additionally, a sensitivity investigation employing a different statistical technique known as RSM is carried out to show how Ra, Ha, and ϕ affect the Nu_{av}. A best-fitted regression equation for the independent factor and response function can be predicted by this numerical simulation on a natural convective wavy square enclosure with a semicircular heater. Additionally, 2D and 3D response function visualizations can be used to illustrate the significance of incorporating nanoparticles into base fluid.

4.1. Influence of Rayleigh Number (Ra)

The influence of Ra from 10^3 to 10^5 on fluid velocity and heat transmission is shown by the streamline and isotherm contours in Figure 4 when $Ha = 10$, $Pr = 6.9$, and $\phi = 0.01$ are held constant. Here, Figure 4(a) illustrates how Ra affects streamlines. It reveals that for low Ra values, the streamlines are nearly identical (dumbbell) at the cavity's vertical midpoint. It is evident that when the Ra changed from 10^3 to 10^5, the streamline pattern remained almost identical, but the velocity field rose enough. However, there are significant differences in the streamlining trend at higher Ra (10^5). A noticeably greater buoyancy effect caused the convective mode of heat transmission around the heater to progressively become stronger. The streamlines have now reached the top from the bottom. In addition to the two revolving rolls on either side of the semicircular heater, two tiny vortices are created inside the main vortex.

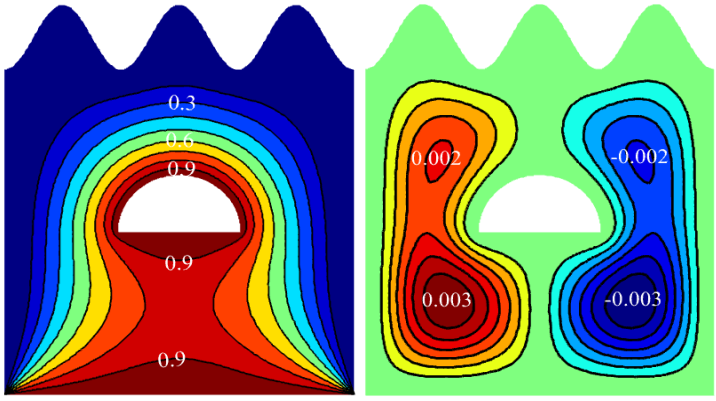

$Ra = 10^3$

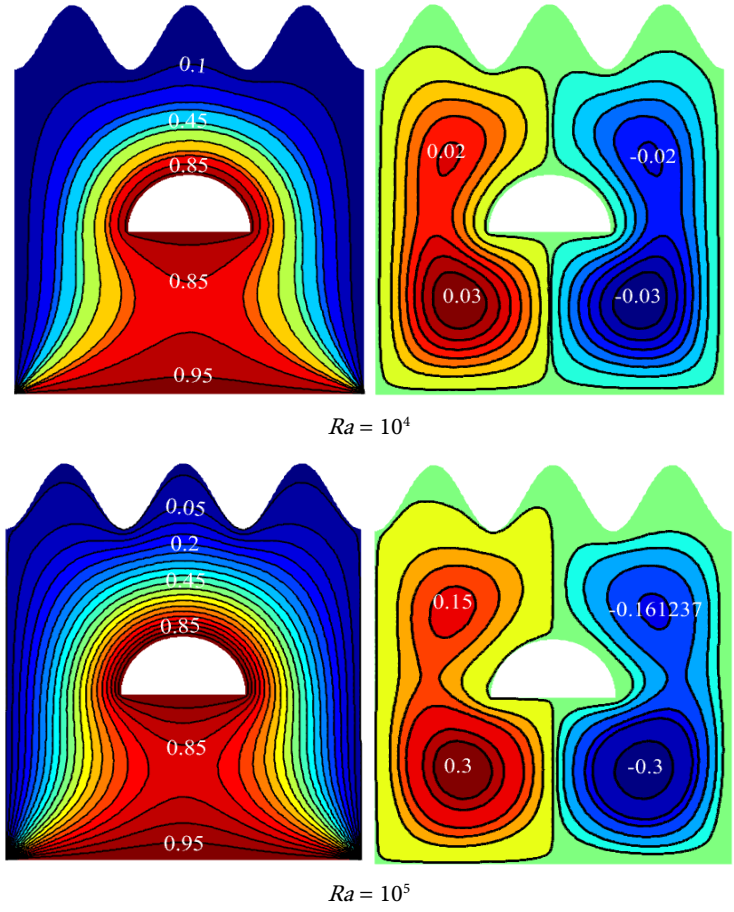

Figure 4. Streamlines and Isotherms for $Ra = 10^3, 10^4, 10^5$ while $Ha = 10$, $Pr = 6.9$ and $\phi = 0.01$.

These vortices demonstrate that at high *Ra* values, massive convection takes place.

The temperature transmission mechanism (conduction or convection) and the useful advantages of temperature, however, are illustrated by the isotherm outlines. **Figure 4(b)** shows how the isotherm's outlines are impacted by Rayleigh's number. The fact that the isotherm contours at the cavity's center are almost parallel along the vertical axis indicates that convection is reduced within the cavity when *Ra* is low (10^3). Weakly convective temperature flow is indicated by the hollow center's low isotherm compactness. The isotherm contours become unduly distorted and start to flatten from hot to cool wall as *Ra* rises. Also, they nearly flatten out at high *Ra* (10^5). The actual reason for this is a rise in *Ra* that causes the fluid velocity to increase. Consequently, convective heat transmission from the hot round exterior on the right to the colder circular exterior on the left occurs naturally. The rate of heat transfer is comparatively lower for low *Ra* (10^3 – 10^4) values, while the change in heat is quite substantial at high *Ra* (10^5) values. Similar findings were also reported by [12] [27].

4.2. Impact of Hartmann Number (*Ha*)

The effect of *Ha*, which represents the magnetic field's influence, is shown in Figure 5 using streamlines and isotherms to preserve $\phi = 0.01$, $Pr = 6.9$, and $Ra = 10^3$. Figure 5(a) shows the streamline fluctuation for various values of *Ha*. The illustrations show a similar symmetric pattern along a vertical line at the streamlines' center for every value of the *Ha* taken into account. Additionally, the streamlines are in their maximum state at $Ha = 0$, when there is no exterior magnetic field present. However, when *Ha* (20, 50, and 100) increases, the streamlines progressively vanish in response to an external magnetic field acting on the system, indicating that the flow intensity decreases as the magnetic field strength increases. This conclusion has physical relevance because a higher field interacts with a moving fluid that has magnetic impressionability and decreases flow movement inside the cavity when an external magnetic field is generated. Furthermore, the streamlines inside the hollow are weakened because the Lorentz force created by applying a magnetic field has a propensity to oppose fluid movement. Moreover, Figure 5(b)'s isothermal lines indicate a change, albeit it is not particularly apparent for bigger *Ha* (50 and 100). This has an actual meaning since the applied magnetic field limits fluid flow. As can be seen from Figure 5(b), the isothermal lines vary very little as a result, and the heat convection brought on by the flow is negligible. Similar findings were also reported by [27].

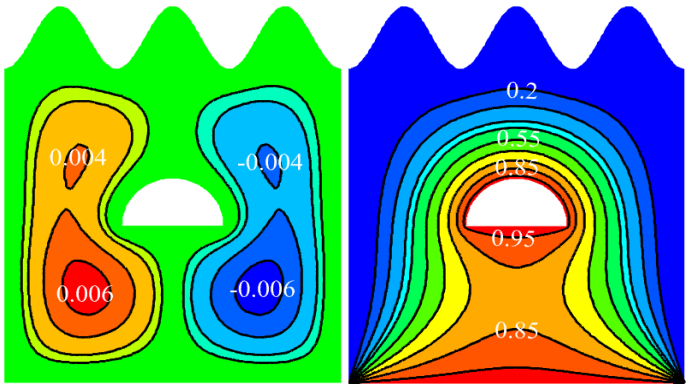

Ha = 0

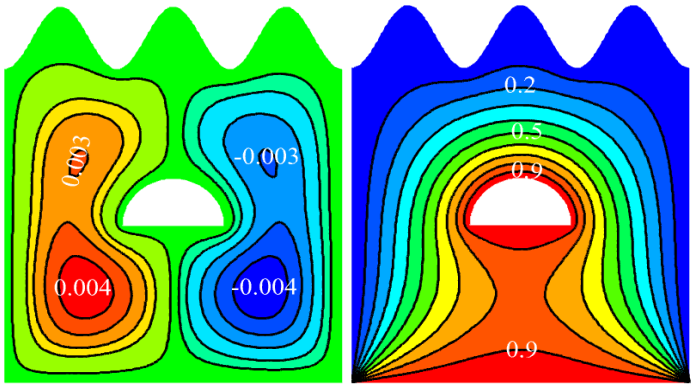

Ha = 20

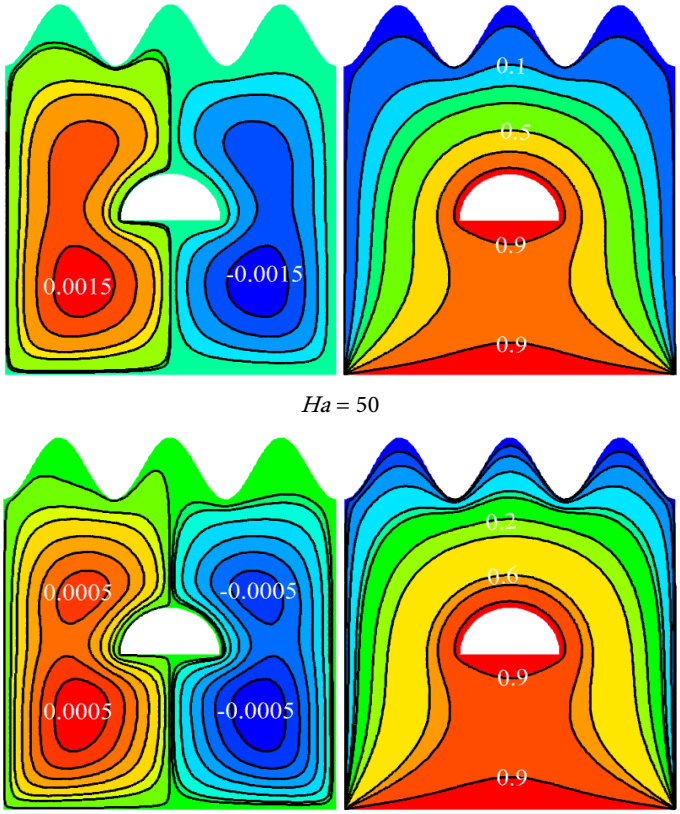

Ha = 50

Ha = 100

(a) (b)

Figure 5. Streamlines and Isotherms for $Ha = 0, 20, 50, 100$ while $Ra = 10^3$, $Pr = 6.9$ and $\phi = 0.01$.

4.3. Impact of Nanoparticle Volume Fraction (φ)

Figure 6 illustrates how the nanoparticle volume fraction (ϕ) affects the streamline and isotherm contours for values of $Pr = 6.9$, $Ha = 10$, and $Ra = 10^3$. The fluid velocity behavior is depicted by streamline contours in **Figure 6(a)**. An increase in ϕ results in increased friction with the base fluid. Consequently, the base fluid's flow encounters a barrier. Thus, as can be seen in **Figure 6(a)** (the streamline from top to bottom), the fluid velocity moves downward.

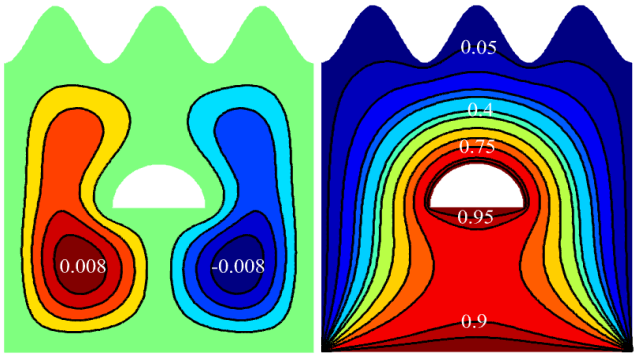

$\phi = 0$

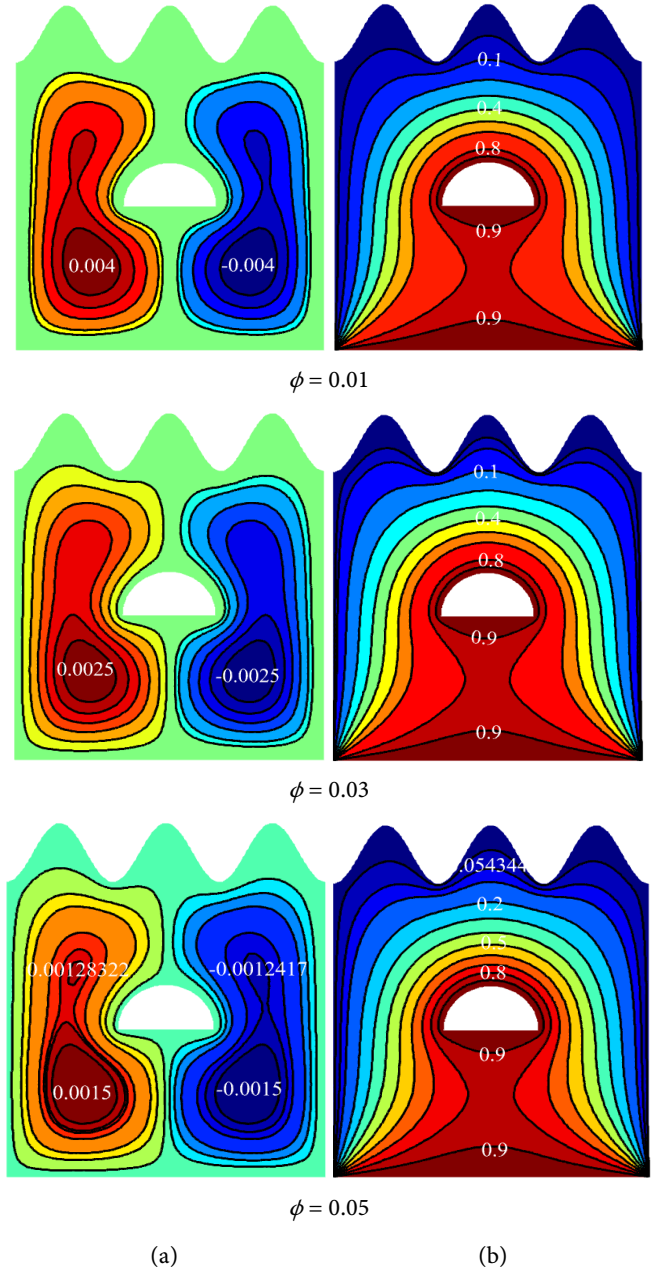

Figure 6. Streamlines and Isotherms for $\varphi = 0, 0.01, 0.03, 0.05$ while $Pr = 6.9$, and $Ra = 10^3$.

A column graph for a specific heat transfer position is displayed in **Figure 6** to provide a more thorough explanation of this effect. In other words, the velocity profile gradually decreases as the size of the nanoparticles increases. Moreover, isotherm contours in **Figure 6(b)** provide a pictorial explanation of the impact on the temperature profile for $\phi = 0, 0.01, 0.03$, and 0.05. It is evident from **Figure 6(b)** that the heat transport gradually becomes stronger as ϕ increases. The physical explanation for this phenomenon is that the thermal conductivity of the nanofluid increases as the volume percentage of nanoparticles increases. The heat transfer rate is therefore higher than it was before. The heat transfer rate (Nu_{av}) is 7.3238 for $\phi = 0$ in the absence of nanoparticle addition in the wavy square cavity.

However, at = 0.01 the rate of heat transfer, shown by isotherm lines, progressively increases from the left hot surface to the right colder surface. The enhanced Nu_{av} in this instance (7.4227) is 1.3% higher than the prior one. The subsequent higher values of $\phi = 0.03$ and $\phi = 0.05$ exhibit the same symptoms. Furthermore, with a 10% increase in the volume fraction of nanoparticles (*i.e.*, for $\phi = 0.01$), the rate of heat transfer from the hot surface to the cool surface is the highest (Nu_{av} = 8.2084). At that point, the rate of heat transmission is likewise 12.2% faster than when there are no nanoparticles present ($\phi = 0$) in this area.

4.4. Influence of Undulation Number (N)

Figure 7(a), Figure 7(b) depict the influence of undulation number on streamlines and isotherms at $Ra = 1000$, $Pr = 6.9$, and $\phi = 0.01$. The flow field comprises multiple circulation cells, indicating the dominance of buoyancy-driven convection. For $N = 0$, a primary clockwise vortex forms along the top, bottom, and upper-left walls. As the number of undulations increases, the wavy geometry disrupts fluid motion, generating multiple vortices with varying orientations. The isotherm patterns for $N = 0$ - 4 reveal plume-like structures originating from the left wall and spreading throughout the cavity. The inner obstacle also contributes to heat distribution. Except for minor variations near the right side of the wavy bottom wall, undulation number has limited impact on overall thermal and flow structures. With higher undulations, additional vortices appear near the right corner, enhancing convective activity.

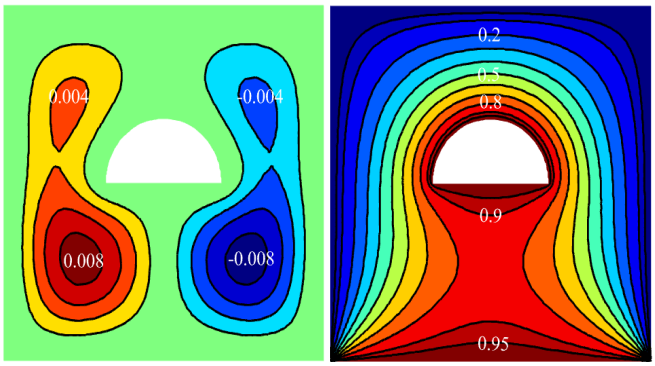

$N = 0$

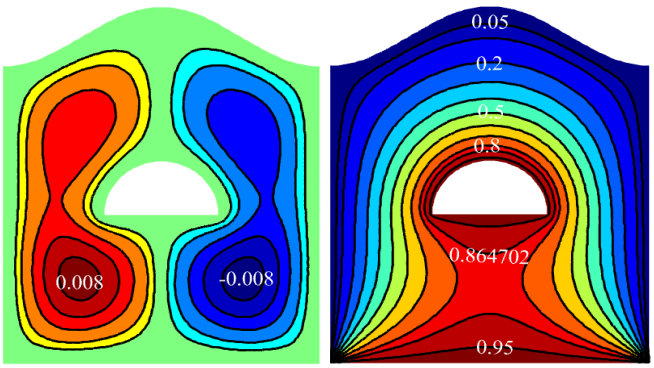

$N = 1$

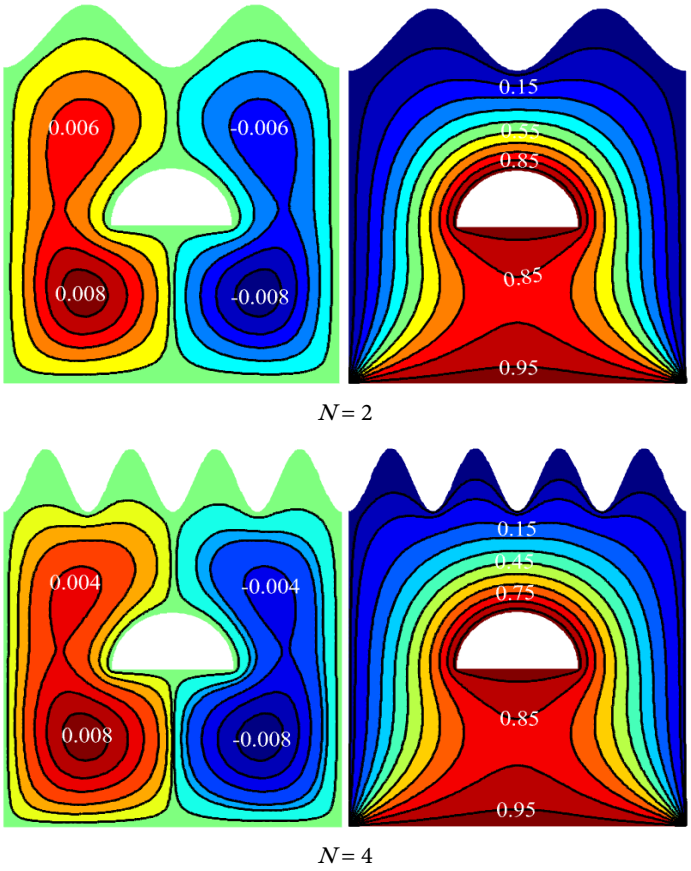

Figure 7. Streamlines and Isotherms for $N = 0, 1, 2, 4$ while $Pr = 6.9$, and $Ra = 10^3$.

A counterclockwise vortex forms at the lower-left corner, and the case $N = 3$ exhibits the most efficient heat transfer. Although increasing undulations reduces the effective cavity area, $N = 3$ provides optimal fluid motion and thermal performance.

4.5. Influence of Nanoparticle Volume Fraction

Figure 8, **Figure 9** portrays the average Nusselt number (Nu_{av}) is analyzed to evaluate the effects of *Ra* and *Ha* on the heat transfer rate for different fluids. **Figure 8** illustrates the variation of Nu_{av} with *Ha* for both pure water and Al_2O_3-H_2O nanofluid. It is evident that Nu_{av} decreases progressively with increasing *Ha*, indicating the suppressive influence of the magnetic field on convective heat transfer. Compared to pure water, the Al_2O_3-H_2O nanofluid exhibits enhancements of 19.82% in Nu_{av}, and overall, its heat transfer rate is 22.62% higher than that of water.

As shown in **Figure 9**, Nu_{av} increases monotonically with rising *Ra* for both fluids, reflecting the dominance of buoyancy effects at higher Rayleigh numbers. The Al_2O_3-H_2O nanofluid demonstrates an additional 15.62% increase in Nu_{av}, confirming its superior thermal performance compared to the base fluid.

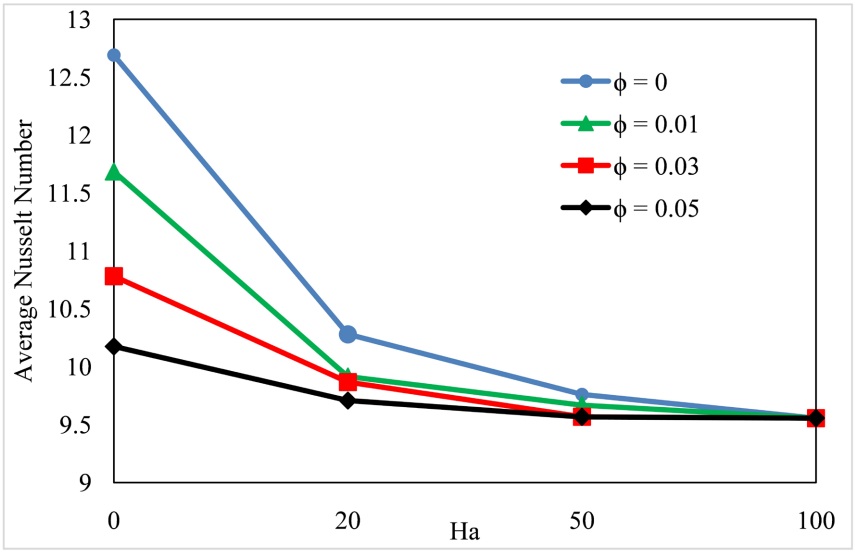

Figure 8. Influence of φ and Ha on Nu_{av}.

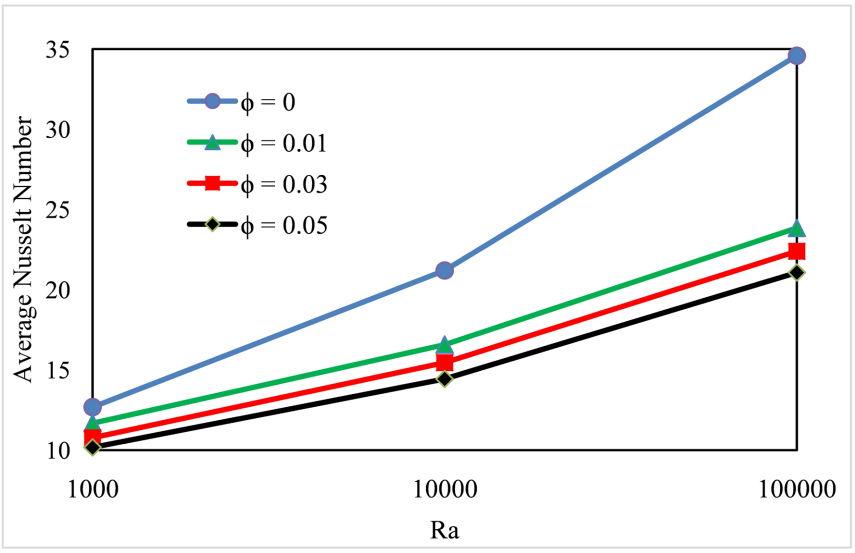

Figure 9. Influence of φ and Ra on Nu_{av}.

4.6. Response Surface Methodology

The statistical RSM technique explains the influence of the important factors (Ha, Ra, and ϕ) Nu_{av} on the response function. Response system modelling (RSM) is one of the best techniques for simulating multifaceted scenarios in which input factors concurrently influence the attention-grabbing responses [21] [25]. The second-order RSM model frequently offers a sufficient approximation of the response, despite the fact that there are several RSM models. Some claim that the quadratic RSM model is:

$$y = \beta_0 + \sum_{i=1}^{3} \beta_i x_i + \sum_{i=1}^{3} \beta_{ii} x_i^2 + \sum_{i=1}^{3} \beta_{ij} x_i x_j \tag{15}$$

In this model, the intercept term is represented by β_0, the response function

(output) by y, the linear regression coefficient of the ith factor by β_i, the quadratic coefficient of the ith factor by β_{ii}, and the interaction coefficient between the ith and jth factors by β_{ij}. The independent variables considered are Ha, ϕ, and Ra, while the Nu_{av} serves as the response variable (y). The main objective is to establish the best-fit correlation between the response and the independent factors.

A second-order Response Surface Methodology (RSM) model based on the Central Composite Design (CCD) is employed [21]. The independent parameters Ra, Ha, and ϕ are varied within specified ranges, and the CCD framework includes 20 experimental runs (8 factorial, 6 axials, and 6 center points). Table 5 presents the coded levels of these parameters, while Table 6 lists both the coded and actual values used in the simulations.

Table 5. CCD strategy factors and coded levels.

Factors	Level		
	−1 (lowest)	0 (medium)	1 (highest)
Ha	0	50	100
Ra	10^3	50,500	10^5
ϕ	0	0.025	0.05

Table 6. Range of input factors and corresponding response variable.

Run Order	Codded Values			Real Values			Response
	A: Ha	B: Ra	C: ϕ	Ha	Ra	ϕ	Nu_{av}
1	0	0	0	50	50,500	0.025	10.1009
2	−1	0	0	0	50,500	0.025	10.368
3	0	−1	0	50	1000	0.025	9.9832
4	0	0	0	50	50,500	0.025	10.1009
5	0	1	0	50	100,000	0.025	10.3597
6	0	0	0	50	50,500	0.025	10.1009
7	1	1	−1	100	100,000	0	12.4637
8	0	0	1	50	50,500	0.05	10.051
9	−1	−1	−1	0	1000	0	12.614
10	−1	1	1	0	100,000	0.05	10.4241
11	−1	−1	1	0	1000	0.05	9.9834
12	0	0	0	50	50,500	0.025	10.1009
13	1	−1	1	100	1000	0.05	9.9831
14	0	0	−1	50	50,500	0	15.0631
15	−1	1	−1	0	100,000	0	34.5921
16	0	0	0	50	50,500	0.025	10.1009
17	1	−1	−1	100	1000	0	9.5552
18	1	0	0	100	50,500	0.025	9.9987
19	0	0	0	50	50,500	0.025	10.1009
20	1	1	1	100	100,000	0.05	10.0372

The outcomes of the statistical analysis using RSM are shown in Table 7. The degrees of freedom (DOF) in this model indicate the maximum number of independent terms. The total sum of squares is one way to depict the entire variance brought about by multiple factors. The significant value of the Adj. SS is 446.53. The Nu_{av} model is statistically significant, as indicated by the F-value of 7.31, which shows that noise does not affect the outcomes. Additionally, a particularly significant signal of this statistical analysis is the p-value, which establishes the probability that the null hypothesis would hold for a particular statistical model. A suitable anticipated outcome is indicated by a small p-value, usually less than 0.05.

Table 7. Analysis of variance for Nu_{av}.

Source	DOF	Adj. SS	F-Value	p-Value	Comment
Model	9	446.53	7.31	<0.0014	**Significant**
Ra	1	66.35	6.51	<0.0241	
Ha	1	67.31	6.61	<0.0233	
ϕ	1	114.31	11.22	0.0052	
Ra^2	1	0.5154	0.0690	**0.7982**	
Ha^2	1	0.542	0.0728	**0.7928**	
ϕ^2	1	21.85	2.92	**0.1181**	
Ra Ha*	1	47.32	4.65	0.0504	
*Ra** ϕ	1	74.37	7.30	0.0181	
*Ha** ϕ	1	76.88	7.55	0.0166	
Lack-of-Fit	5	74.75	-	-	**Insignificant**
Pure Error	5	0.000	-	-	
Total	19	578.92	-	-	

**Here, R^2 = 87.09%, Adjusted R^2 = 75.47%.

Table 7 makes clear how crucial each input piece is to this strategy. Additionally, good R^2 (87.09%) values for Nuav are shown by the model statistical analysis and testing procedures, suggesting that this model is suitable for determining the Nu_{av} response function. Despite being less than R^2 (75.47%), the model's improved R^2 (87.09%) nevertheless well describes the experimental data. Lack of Fit is another crucial statistic that requires very little in the way of a good model. To investigate the association between the response (Nu_{av}) and the effective input parameters (*Ra*, *Ha*, and ϕ), RSM developed the following general models:

$$y = z_0 + z_1 Ra + z_2 Ha + z_3 \phi + z_{11} Ra^2 + z_{22} Ha^2 + z_{33} \phi^2 + z_{12} Ra \cdot Ha + z_{13} Ra \cdot \phi + z_{23} Ha \cdot \phi \quad (16)$$

In this model, $z_0, z_1, z_2, z_3, z_{11}, z_{22}, z_{33}, z_{12}, z_{13}$ and z_{23} denote the coefficients

of the best-fitted regression equation obtained from the RSM analysis. The coded variables employed to estimate the predicted coefficients of Equation (16) for Nu_{av} are presented in Table 8. Only those terms with low p-values (≤0.05) are taken into consideration when creating an appropriate regression equation. Conversely, phrases that are not important are ignored (bold highlighted). That is, Ra, Ha, ϕ, $Ra{\cdot}Ha$, $Ra{\cdot}\phi$, and $Ha{\cdot}\phi$ are key terms for the response function (Nu_{av}). However, Ra^2, ϕ^2, and Ha^2 should not be included in the final best-fitted regression model because they have no effect whatsoever on Nu_{av}.

Table 8. Predicted regression coefficients for Nu_{av} obtained from RSM analysis.

Coefficients	z_0	z_1	z_2	z_3	z_{11}	z_{22}	z_{33}	z_{12}	z_{13}	z_{23}
Values	9.96	−2.59	2.58	−3.38	0.4448	0.4329	2.82	−2.43	3.10	−3.03
p-values	-	<0.0014	<0.0233	0.0241	**0.7982**	**0.7928**	**0.1181**	0.0504	0.0181	0.0166

In the regression model for Nu_{av} (Equation (16)), the quadratic terms Ra^2, Ha^2, and ϕ^2 are found to be insignificant. Hence, the relationship between Nu_{av} and the parameters Ra, Ha, and ϕ can be expressed by the following mathematical form:

$$\begin{aligned} Nu_{av} &= 9.96 - 2.59Ha + 2.58Ra - 3.38\phi + 0.7928Ha^2 + 0.7982Ra^2 \\ &+ 0.1181\phi^2 - 2.43Ha \cdot Ra + 3.10Ha \cdot \phi - 3.03Ra \cdot \phi \end{aligned} \quad (17)$$

Equation (17) represents the best-fitted correlation between Nu_{av} and the independent variables.

4.7. Response Surface Analysis

Figures 10-12 illustrate the 2D and 3D contour plots of the RSM-generated response surface (Nu_{av}), highlighting the effects of the influencing parameters on the response. Figure 10(a) depicts the combined influence of Ra and Ha on Nu_{av}, keeping ϕ fixed at 0.025. The 2D contour map shows that Nu_{av} increases with higher Ra and lower Ha, attaining its maximum at Ra = 1000 and Ha = 0, and its minimum at Ra = 100,000 and Ha = 100. The corresponding 3D surface plot in Figure 10(b) confirms the same trend, consistent with the FEM results. Similarly, Figure 11(a) presents the effect of ϕ and Ha on Nu_{av} at a constant Ra = 1000. An increase in ϕ and a reduction in Ha enhance Nu_{av}, with the highest value at ϕ = 0.01 and Ha = 0, and the lowest at ϕ = 0 and Ha = 100. The 3D surface in Figure 11(b) further supports this observation. Figure 12(a) displays the relationship between Ra and ϕ on Nu_{av} at a fixed Ha = 10. As both Ra and ϕ increase, Nu_{av} also rises, reaching its peak at Ra = 1000 and ϕ = 0.01, and its minimum at Ra = 10^5 and ϕ = 0. The 3D surface plot in Figure 12(b) exhibits a similar trend, reaffirming the consistent behavior of the response surface.

The statistical method RSM is also employed to demonstrate the statistical validity of the results of the applied FEM. The FEM's results are comparable to those of the RSM. The suggested natural convection numerical analysis employing aluminum water nanofluid is highly supported by this agreement.

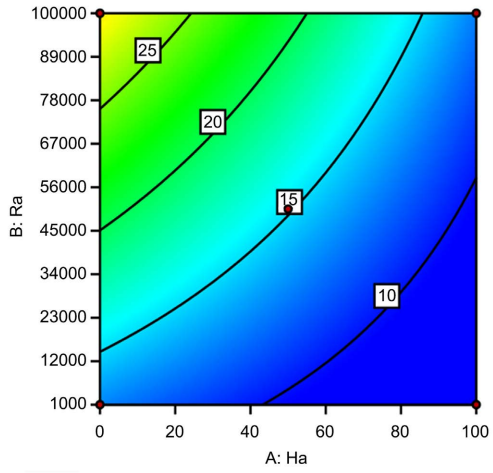

(a)

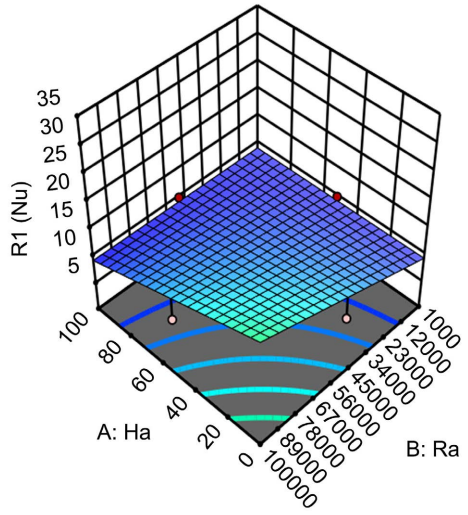

(b)

Figure 10. Effect on Nu_{av} for *Ra* and *Ha*: (a) 2D sight; (b) 3D sight.

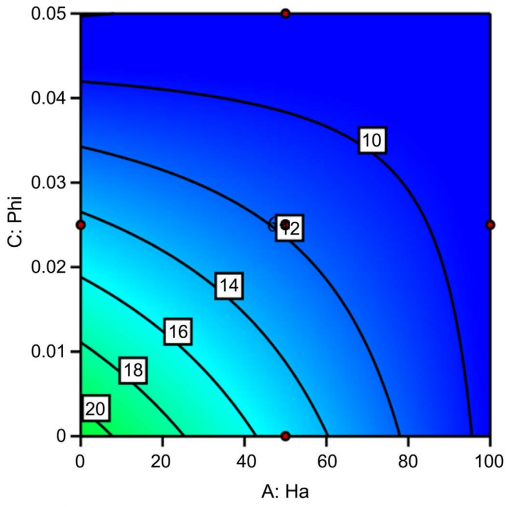

(a)

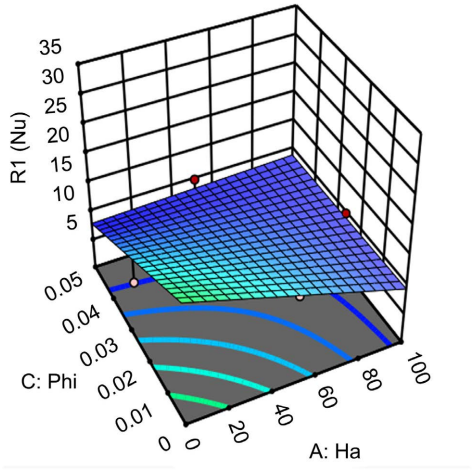

(b)

Figure 11. Effect on Nu_{av} for φ and Ha: (a) 2D sight; (b) 3D sight.

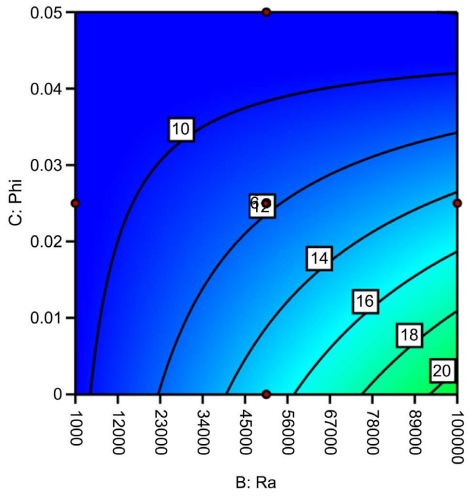

(a)

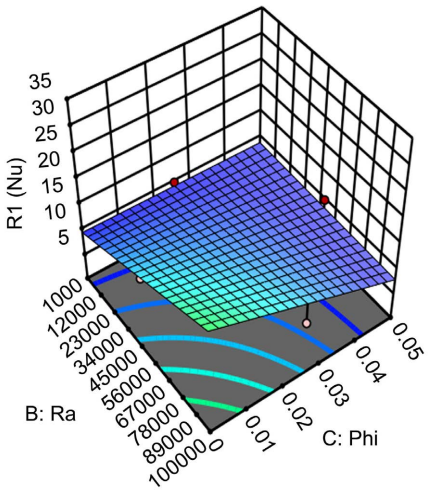

(b)

Figure 12. Effect on Nu_{av} for Ra and φ: (a) 2D sight; (b) 3D sight.

5. Conclusion

This study numerically investigated MHD natural convection of Al_2O_3-water nanofluid in a wavy square cavity with a semicircular heater using FEM and RSM-based optimization. The results revealed that increasing the Rayleigh number strengthens buoyancy-driven convection, leading to a significant rise in heat transfer. For instance, Nu_{av} increased by nearly 12.2% at $\varphi = 0.01$ compared with pure water, confirming the enhanced thermal conductivity effect of nanoparticles. Similarly, at $\varphi = 0.05$, the heat transfer rate improved by about 19.82% relative to the base case. Conversely, stronger magnetic fields (higher Hartmann numbers) suppressed convection due to Lorentz forces, leading to a noticeable reduction in streamline circulation and corresponding decline in Nu_{av}. Also, $N = 3$ shows the most efficient heat transfer and optimal fluid circulation despite reduced cavity area. The RSM analysis confirmed that *Ra*, *Ha*, and φ are statistically significant parameters, with an overall model accuracy of $R^2 = 87.09\%$, validating the robustness of the numerical results. The combined FEM-RSM framework thus provides an effective predictive tool for optimizing nanofluid-based convective systems under magnetic field effects.

Data Availability

The study employs a numerical technique, and no data are employed in the study's findings.

Conflicts of Interest

The authors declare no conflicts of interest regarding the publication of this paper.

References

[1] Sheikholeslami, M. (2022) Modeling Investigation for Energy Storage System Including Mixture of Paraffin and ZnO Nano-Powders Considering Porous Media. *Journal of Petroleum Science and Engineering*, **219**, Article ID: 111066. https://doi.org/10.1016/j.petrol.2022.111066

[2] Uddin, M.J., Al-Balushi, J., Mahatabuddin, S. and Rahman, M.M. (2022) Convective Heat Transport for Copper Oxide-Water Nanofluid in an Isosceles Triangular Cavity with a Rippled Base Wall in the Presence of Magnetic Field. *International Journal of Thermofluids*, **16**, Article ID: 100195. https://doi.org/10.1016/j.ijft.2022.100195

[3] Runa, A.A., Alim, M.A., Alam, M.S. and Kabir, K.H. (2022) Finite Element Analysis of Magnetohydrodynamic Natural Convection within Semi-Circular Top Enclosure with Triangular Obstacles. *American Journal of Computational Mathematics*, **12**, 33-43. https://doi.org/10.4236/ajcm.2022.121004

[4] Bülbül, H., Atalay, T., Yakut, Y., Özbektaş, S. and Köysal, Y. (2025) Investigation of the Effect of Natural Convection Cooling Caused by the Chimney Effect on the Improved Solar Thermoelectric System. *Applied Thermal Engineering*, **263**, Article ID: 125431. https://doi.org/10.1016/j.applthermaleng.2025.125431

[5] Putra, N., Roetzel, W. and Das, S.K. (2002) Natural Convection of Nano-Fluids. *Heat and Mass Transfer*, **39**, 775-784. https://doi.org/10.1007/s00231-002-0382-z

[6] Brinkman, H.C. (1952) The Viscosity of Concentrated Suspensions and Solutions.

The Journal of Chemical Physics, **20**, 571-571. https://doi.org/10.1063/1.1700493

[7] Abu-Nada, E., Masoud, Z., Oztop, H.F. and Campo, A. (2010) Effect of Nanofluid Variable Properties on Natural Convection in Enclosures. *International Journal of Thermal Sciences*, **49**, 479-491. https://doi.org/10.1016/j.ijthermalsci.2009.09.002

[8] Nasrin, R., Alim, M.A. and Chamkha, A.J. (2012) Combined Convection Flow in Triangular Wavy Chamber Filled with Water-CuO Nanofluid: Effect of Viscosity Models. *International Communications in Heat and Mass Transfer*, **39**, 1226-1236. https://doi.org/10.1016/j.icheatmasstransfer.2012.06.005

[9] parvin, S., Nasrin, R. and Alim, M.A. (2014) Heat Transfer Performance of Nanofluid in a Complicated Cavity Due to Prandtl Number Variation. *Procedia Engineering*, **90**, 377-382. https://doi.org/10.1016/j.proeng.2014.11.865

[10] Zahan R, I. and MA Alim, N. (2018) MHD Effect on Conjugate Heat Transfer in a Nanofluid Filled Rectangular Enclosure. *International Journal of Petrochemical Science & Engineering*, **3**, 114-123. https://doi.org/10.15406/ipcse.2018.03.00085

[11] Alsabery, A.I., Tayebi, T., Chamkha, A.J. and Hashim, I. (2018) Effects of Non-Homogeneous Nanofluid Model on Natural Convection in a Square Cavity in the Presence of Conducting Solid Block and Corner Heater. *Energies*, **11**, Article 2507. https://doi.org/10.3390/en11102507

[12] Saha, T., Islam, T., Yeasmin, S. and Parveen, N. (2023) Thermal Influence of Heated Fin on MHD Natural Convection Flow of Nanofluids Inside a Wavy Square Cavity. *International Journal of Thermofluids*, **18**, Article ID: 100338. https://doi.org/10.1016/j.ijft.2023.100338

[13] Rashid, U., Lu, D. and Iqbal, Q. (2023) Nanoparticles Impacts on Natural Convection Nanofluid Flow and Heat Transfer Inside a Square Cavity with Fixed a Circular Obstacle. *Case Studies in Thermal Engineering*, **44**, Article ID: 102829. https://doi.org/10.1016/j.csite.2023.102829

[14] Ibáñez, G., Cuevas, S. and López de Haro, M. (2006) Optimization of a Magnetohydrodynamic Flow Based on the Entropy Generation Minimization Method. *International Communications in Heat and Mass Transfer*, **33**, 295-301. https://doi.org/10.1016/j.icheatmasstransfer.2005.12.003

[15] Islam, T., Alam, M.N., Asjad, M.I., Parveen, N. and Chu, Y. (2021) Heatline Visualization of MHD Natural Convection Heat Transfer of Nanofluid in a Prismatic Enclosure. *Scientific Reports*, **11**, Article No. 10972. https://doi.org/10.1038/s41598-021-89814-z

[16] Jani, S., Mahmoodi, M. and Amini, M. (2013) Magnetohydrodynamic Free Convection in a Square Cavity Heated from Below and Cooled from Other Walls. *International Journal of Mechanical, Aerospace, Industrial, Mechatronic and Manufacturing Engineering*, **7**, 750-755.

[17] Einstein, A. (1906) Eine neue Bestimmung der Moleküldimensionen. *Annalen der Physik*, **324**, 289-306. https://doi.org/10.1002/andp.19063240204

[18] Batchelor, G.K. (2016) The Effect of Brownian Motion on the Bulk Stress in a Suspension of Spherical Particles. *Exercer*, **83**, 40-41.

[19] Xu, G., Fu, J., Dong, B., Quan, Y. and Song, G. (2019) A Novel Method to Measure Thermal Conductivity of Nanofluids. *International Journal of Heat and Mass Transfer*, **130**, 978-988. https://doi.org/10.1016/j.ijheatmasstransfer.2018.11.014

[20] Raja, R.A.A., Sunil, J. and Maheswaran, R. (2018) Estimation of Thermo-Physical Properties of Nanofluids Using Theoretical Correlations. *International Journal of Applied Engineering Research*, **13**, 7950-7953.

[21] Jahan, A., Edwards, K.L. and Bahraminasab, M. (2016) Multi-Criteria Decision Analysis for Supporting the Selection of Engineering Materials in Product Design. Butterworth-Heinemann.

[22] Zheng, N., Liu, P., Liu, Z. and Liu, W. (2017) Numerical Simulation and Sensitivity Analysis of Heat Transfer Enhancement in a Flat Heat Exchanger Tube with Discrete Inclined Ribs. *International Journal of Heat and Mass Transfer*, **112**, 509-520. https://doi.org/10.1016/j.ijheatmasstransfer.2017.05.019

[23] Fereidooni, J. (2023) Baffles' Size Impact on the Heat Transfer and Second Law Features of Magnetic Hybrid Nanofluid within a Hexagonal-Shaped Porous Domain. *Journal of Magnetism and Magnetic Materials*, **582**, Article ID: 171037. https://doi.org/10.1016/j.jmmm.2023.171037

[24] Raizah, Z. and Aly, A.M. (2021) Effect of Dual-Rotation on MHD Natural Convection of NEPCM in a Hexagonal-Shaped Cavity Based on Time-Fractional ISPH Method. *Scientific Reports*, **11**, Article No. 22687. https://doi.org/10.1038/s41598-021-02046-z

[25] Vahedi, S.M., Zare Ghadi, A. and Valipour, M.S. (2018) Application of Response Surface Methodology in the Optimization of Magneto-Hydrodynamic Flow around and through a Porous Circular Cylinder. *Journal of Mechanics*, **34**, 695-710. https://doi.org/10.1017/jmech.2018.1

[26] Islam, T., Gama, S. and Martins Afonso, M. (2024) Artificial Neural Network and Response Surface Methodology-Driven Optimization of Cu-Al_2O_3/Water Hybrid Nanofluid Flow in a Wavy Enclosure with Inclined Periodic Magnetohydrodynamic Effects. *Mathematics*, **13**, Article 78. https://doi.org/10.3390/math13010078

[27] Islam, S., Bairagi, T., Islam, T., Rana, B.M.J., Reza-E-Rabbi, S. and Rahman, M.M. (2022) Heatline Visualization in Hydromagnetic Natural Convection Flow Inside a Prismatic Heat Exchanger Using Nanofluid. *International Journal of Thermofluids*, **16**, Article ID: 100248. https://doi.org/10.1016/j.ijft.2022.100248

[28] Rahman, M.M., Öztop, H.F., Joarder, A.H., Saidur, R., Hamzah, N., Al-Salem, K. and Ibrahim, T.A. (2016) Unsteady Analysis of Natural Convection in a Carbon Nanotube-Water Filled Cavity with an Inclined Heater. *Numerical Heat Transfer*, *Part A*: *Applications*, **69**, 794-809. https://doi.org/10.1080/10407782.2015.1090825

[29] Garnett, J.C.M., (1904) Colours in Metal Glasses and in Metallic Film. *Proceedings of the Royal Society of London*, **203**, 359-371.

[30] Ghasemi, B., Aminossadati, S.M. and Raisi, A. (2011) Magnetic Field Effect on Natural Convection in a Nanofluid-Filled Square Enclosure. *International Journal of Thermal Sciences*, **50**, 1748-1756. https://doi.org/10.1016/j.ijthermalsci.2011.04.010

Nomenclature

B_0	Applied magnetic field
C_p	Fluid specific heat
d	Diameter of particle
g	Gravitational acceleration
H	Enclosure height
Gr	Grashof number
k	Fluid thermal conductivity
$\overline{Nu}$	Average Nusselt number
p	Fluid pressure
P	Non-dimensional pressure of the fluid
Pr	Prandtl number
Ha	Hartmann number
Nu	Nusselt Number
Ra	Rayleigh number
T	Temperature
T_c	Cold temperature
T_h	Heated temperature
ΔT	Temperature difference
u, v	Dimensional velocity components
U, V	Dimensionless velocity component
x, y	Dimensional Cartesian coordinates
X, Y	Dimensionless Cartesian coordinates
Greek Symbols	
α	Fluid thermal diffusivity
β	Coefficient of thermal expansion of fluid
μ	Fluid dynamic viscosity
ν	Fluid kinematic viscosity
σ	Fluid electrical conductivity
θ	Dimensionless temperature
ρ	Density of the fluid
φ	Nanofluid Volume Fraction
Subscripts	
c	cold
h	heated
nf	Nanofluid
f	Base fluid (water)
s	Nanoparticles
av	Average